Numerical simulations of the autorotative flight of the real and artificial maple seeds

Myong H. Sohn[1,*], Han S. Yoo[2], Joun G. Kwak[1]

[1]Department of Aeronautical and Mechanical Engineering, Cheongju University, Cheongju, Republic of Korea
[2]School of Mechanical Engineering, Sungkyunkwan University, Suwon, Republic of Korea
*corresponding author: myongsohn@hanmail.net

Abstract Autorotative flight of plant seeds is the result of the delicate equilibrium between gravity (weight of the seed), inertial force as well as aerodynamic force. This study performed numerical simulations of the autorotative flight of real and artificial maple seeds. The 3-dimensional (3D) configuration data of the real maple seed were obtained by using 3D optical scanning, and they were used in the calculation of the aerodynamic force acting on the seed, and to solve the 6-degree-of-freedom (6DOF) motion in the autorotative flight. The motion parameters such as the descent velocity, the spinning rate, and the coning angle agreed reasonably well with those measured for real sample seeds. 6DOF simulation of the artificial maple seeds was also performed to investigate the effect of the position of center of gravity on the autorotative flight of maple seeds. It was found that the chordwise position of the center of gravity, which determines the moment about the span axis and consequently governs the pitch angle, was the most influential factor of the configuration characteristics in the autorotative flight of maple seeds. The result of the present study confirms several facts and assumptions for the autorotative flight of plant seeds reported in the previous studies.
Keywords: autorotative flight, maple seed, numerical simulation, 6-degree-of-freedom motion

1 Introduction

Seed dispersal is an important process for species reproduction of plants by enabling embryo-bearing seeds to settle and grow in a suitable location away from their parental plants [1]. Various forms of seed dispersal exist, including hitchhiking on animals, self-explosion, drifting in water, and wind dispersal. Specifically, two kinds of wind dispersal are available, namely, papoose seeds (parachute type) and winged seeds. Papoose seeds use drag force acting on the pappi, whereas winged seeds mainly utilize lift force acting on the wings. Some winged seeds (maple tree, ash tree, tipu tree, etc.) autorotate during their fall to slow down their descent velocity and be windblown far away from their parent trees [2]. Autorotating seeds reportedly have much higher wing loading compared with seeds assuming other types of wind dispersal. For example, the wing loading of some autorotating seeds is 450% higher than that of gliding and straying seeds) [3]. The much higher wing loading with a slightly increased descent speed of autorotating seeds indicates that the autorotation dispersal can carry a weight more efficiently than the glide and straying dispersal.

Autorotative flight of plant seeds is the result of a delicate equilibrium between gravity (weight of the seed) and inertial as well as aerodynamic forces. In the steady vertical flight of an autorotating seed, the vertical component of aerodynamic force and the weight of the seed are balanced, as are the resistant and driving torques. Figure 1 shows the forces and the motion parameters of autorotative flight of plant seeds. Even in the vertical descent of an autorotating seed, the seed blade plane is not perpendicular to the vertical spinning axis. The tangent plane to the conical surface swept by the seed blade (flight path plane in this study) makes an angle β with the horizontal plane, and this angle is defined as the coning angle (Fig. 1a). The coning angle ranges from 15° to 30° for maple seeds [4]. The angle between the flight path plane and the chord line of the blade is called as the pitch angle θ (Fig. 1b). The positive direction of the pitch angle is defined as the nose-up direction in the present study. The flight path plane makes an angle of $\tan^{-1}(V_D\cos\beta/r\Omega)$ with r as the radial distance from the spinning center because the resultant relative wind is the vector sum of the rotational velocity ($V_H = r\Omega$) and the descent velocity component ($V_D\cos\beta$). This angle is represented by φ in Fig. 1b. Therefore, the local angle of attack α of the local blade section becomes $\varphi+\theta$.
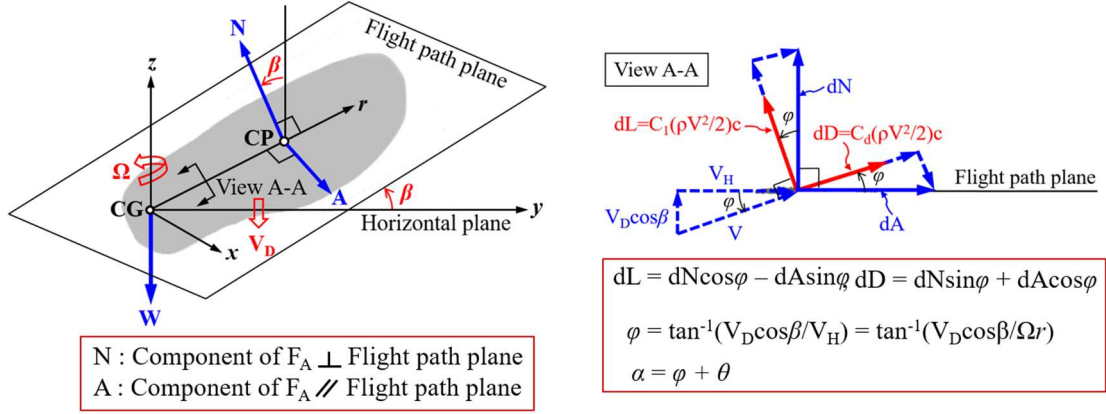
Fig. 1 Forces and motion parameters of autorotative flight

The aerodynamic forces dL and dD and the angle φ are functions of the radial coordinate r. The driving torque is expressed as $r\mathrm{dL}\sin\varphi$, whereas the resisting torque is $r\mathrm{dD}\cos\varphi$. dL denotes the lift component acting on the blade section of infinitesimal span dr, and dD is the drag component acting on dr. The rotational velocity of autorotation accelerates as the magnitude of $(\mathrm{dL}\sin\varphi - \mathrm{dD}\cos\varphi)$ becomes positive. The steady descent and rotational velocities of an autorotating seed indicate that the seed automatically adjusts its pitch and coning angles to establish a stable equilibrium angle φ with balancing aerodynamic forces. The forces and moments based on the notations shown in Fig. 1 are as follows.

− Forces in the vertical direction:

$$\int_{r=-R_b}^{r=R_t} \left(\mathrm{dL}\cos\varphi + \mathrm{dD}\sin\varphi\right)\cos\beta\, dr - W = 0 \tag{1}$$

− Moment about the spinning axis in the flight plane:

$$\int_{r=-R_b}^{r=R_t} \left(\mathrm{dL}\sin\varphi - \mathrm{dD}\cos\varphi\right) r\cos\beta\, dr = 0 \tag{2}$$

− Moment about the flapping axis:

$$+\int_{r=-R_b}^{r=R_t} \left(\mathrm{dL}\cos\varphi + \mathrm{dD}\sin\varphi\right) r\, dr$$
$$-\int_{r=-R_b}^{r=R_t} \left(\rho_w dr\right)\left[\left(\Omega^2 r^2 \cos^2\beta\right)/\left(r\cos\beta\right)\right]\left(\sin\beta\right) r$$
$$-\int_{r=-R_b}^{r=R_t} g\left(\rho_w dr\right)\left(\cos\beta\right) r = 0 \tag{3}$$

where the upper limit of the integration (R_t) is the distance between the spinning axis of autorotation and the wing tip of the seed and R_b is the distance between the spinning axis and the base tip of the seed. The total span (b) of the seed blade is the sum of R_t and R_b. R_b is usually very small compared with R_t for most maple seeds. In Eq. (3), the first term is the moment generated by the aerodynamic force, the second term is the moment caused by the centrifugal force, and the third term is the moment formed by the distributed weight of the seed. The aerodynamic force dominated by the lift component functions as the moment of increasing the coning angle. The other two forces act as the moment of decreasing the coning angle.

Many scientists investigated phenomena of autorotating plant seeds. Norberg [5] investigated the transient stage of entering autorotation and the stability of the autorotation of winged seeds. Influences of geometric parameters such as the planform and mass distribution, and aerodynamic properties were examined, and the concentration of vascular bundles at the leading edge of the seed wing and the tapering of the wing thickness towards the trailing edge were considered to be essential for a proper chordwise mass distribution. The momentum and blade-element theories were employed in extracting the aerodynamic properties. Norberg showed that autorotating descent possesses static and dynamic stability, and that the aerodynamic and

centrifugal forces interacted so as to give pitch stability.

Azuma and Yasuda [4] presented extensive data for geometrical configurations of autorotating plant seeds and their flight characteristics. Azuma and Yasuda showed that the flight characteristics such as the descent velocity, spinning rate, pitch angle and coning angle were dependent on the configuration characteristics such as the area and mass of the seed, the wing section configuration, and the position of center of gravity (CG). Especially, it was reported that the descent velocity was in proportion to the square root of the wing loading. Yasuda and Azuma [6] suggested that the downwardly convex mean camberline of the seed wing section at least near the wing root (or near the CG location) is essential for stable autorotation with low descent velocity and high spinning rate, and the surface roughness increases the spinning torque. They also argued that the planform is less influential factor for governing the flight behavior of autorotating plant seeds, compared to other geometrical characteristics such as the section geometry and the CG location. Seter and Rosen [7] gave a detailed information for the autorotative flight of winged seeds employing the six degrees-of-freedom motion analysis and the aerodynamic force data based on the blade-element and momentum theory. The values of sectional lift and drag coefficients were estimated from available insect wing's data. Seter and Rosen employed CG-adjustable artificial wing models to verify the theoretical analysis and deduce the effects of various aerodynamic parameters such as the axial and tangential induced velocities, the tip effects, the chordwise location of center of pressure, the spanwise flow effect, and the drag force of the root region. They showed that the cross-sectional lift and drag coefficients greatly influenced the motion parameters of the autorotative flight. They concluded that autorotation of a single-winged plant seed was a highly nonlinear phenomenon representing a delicate equilibrium between gravity, inertia and aerodynamic effects.

Lentink et al [3] and Lee et al. [8] presented detailed experimental data for the aerodynamics of the autorotative flight of plant seeds. Lentink et al. measured the flow around dynamically scaled robotic models. The flight parameters and the ratio of inertial to viscous stress in the surrounding flow of the model seeds in mineral oil tank were scaled such that they are identical to real seeds descending in air. Stereo digital particle image velocimetry (DPIV) was used to measure the 3D velocity field around the artificial seeds. Stable leading-edge vortex (LEV) was found to exist on the leeward surface of the autorotating seed, and it was accounted to be the ultimate source of the high lift generated in the autorotating plant seeds studied. They also argued that the attached stable LEV was possible by the intense spanwise flow and spanwise transport of vorticity. Lee et al. [8] measured the flow field of the autorotating actual seed suspended in the vertical wind tunnel using DPIV. They confirmed the attached and stable LEV on the leeward surface, and provided a detailed information of the flow field around the autorotating sample seed such as the streamwise velocity profile, and the spanwise and vertical positions of LEV center. Varshney et al. [9] investigated experimentally the kinematics of the free-falling maple seeds by varying the level of cutting the natural maple seed from the intact seed to the seed with only a sliver of leading edge. They observed that the seed with only a sliver of leading edge could still autorotate, and free-falling maple seeds reached a stable autorotation after two transient states, tumbling about the spanwise direction and rotation about the vertical axis through the tilting towards the vertical axis.

Recently Lee and Choi [10] and Arranz et al. [11] performed numerical simulations of the autorotative flight of winged seeds. Lee and Choi conducted numerical simulation of free-falling maple seed using an immersed boundary method in a non-inertial reference frame. A three-dimensional configuration data obtained by scanning the real maple seed (*Acer palmatum*) was used as the body geometry in the numerical simulation. They analyzed the flow characteristics of the autorotating maple seed such as the behavior of the leading edge, trailing edge, wing-tip, and wing-root vortices during the transient period and the stable periodic rotating period. Arranz et al. performed a numerical simulation of the autorotative flight of a model winged seed. They used an artificial seed by simplifying the shape of a natural *Tipuana Tipu* seed to the level of defining the geometry analytically (the seed wing was defined as a combination of four quarters of ellipse and the nut as an oblate spheroid). They solved simultaneously the Navier-Stokes equations for the flow surrounding the seed and the rigid-body equation for the motion of the seed. Arranz et al. especially focused on the effect of the Reynolds number on the motion parameters of the autorotative flight and the aerodynamic forces generated. The range of Reynolds number considered in the reference 11 was from 80 to 240, which was considered to be the lower limit of Reynolds number in the autorotative flight of plant seed.

The autorotative flight of plant seeds is carried out through the fixed configuration, which is different

from the wings of birds and insects which are deformable and controllable. Therefore, it can be said that the configuration characteristics solely determines the motion characteristics of the autorotative flight of plant seeds. The present study performed a numerical simulation of the autorotative flight of real and artificial maple seeds to reveal the interrelation between the configuration characteristics and the motion characteristics of the autorotating plant seeds. The flow field around the seed and the aerodynamic forces acting on the seed were calculated by using the Navier-Stokes equations and the 6-degree-of-freedom (6DOF) motion of the autorotating seed was solved simultaneously.

2 Material and methods

2.1 Measurement of sample seed geometry and motion parameters

Sample seeds in a natural fallen condition were collected in Mid-October and November, and they were preserved in a plastic box sealed with paraffin to conserve their water content. The mass of the sample seeds was measured just before the experiment using an electronic balance (OHAUS AP2500 Analytical Plus; accuracy=0.01 mg). The span, chord, and planform area of the sample seeds were measured from the enlarged photo images. The mass of the sample seed was 33 mg. The total span of the seed was 22.8 mm, and the planform area of the seed was 130.5 mm^2. Therefore, the wing loading of the sample seed, which is an important parameter of the autorotative flight of the plant seed, was calculated to be 2.84 N/m^2. This value is within the range of wing loading of maple seeds having similar size reported in the previous studies [2][3][4][5]. Three-dimensional (3D) optical scanning was employed to obtain the 3D morphology of the sample seeds. Figure 2 shows the sample seed image and the dimension of the configuration elements. The thickness distribution of the sample seed, which was obtained from the 3D optical scanning, is also presented in Fig. 2.

Mass (m)=33 mg, Span (b)=22.8 mm, Maximum chord (C_{max})=7.45 mm, Planform area (A) =130.5 mm^2, Mean chord (C)=A/b=6.98 mm, t_{max}=3.2 mm, Wing loading (W/A)=2.48 N/m^2
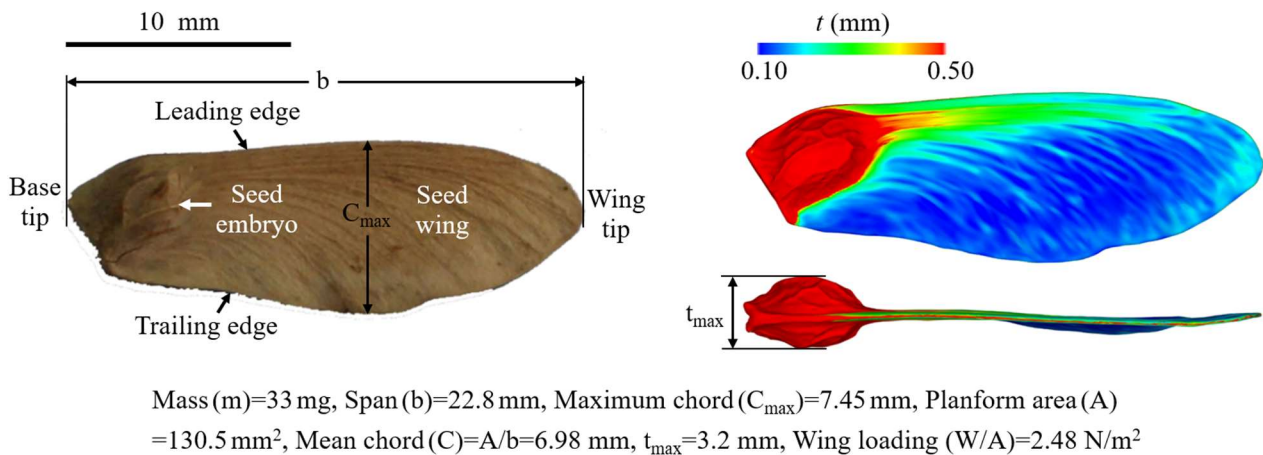
Fig. 2 Sample maple seed and its dimension

The motion parameters of autorotative flight of sample seeds were measured using a high-speed camera (Photron Fastcam Ultima APX). Free-fall tests were performed in a closed chamber to avoid any disturbance. The average descent speed, spinning rate, and coning angle of the sample maple seeds were 0.905 m/sec, 130.0 rad/sec, and 23.2°, respectively. The pitch angle was not measured due to its small value.

2.2 Improved CG calculation

Previous numerical simulations of the autorotative flight of the maple seeds usually assume a uniform density throughout the whole seed and considered the volume centroid of the seed as the CG point (for example [10]). This procedure may lead to an inaccurate CG point, which is the utmost configuration parameter characterizing the autorotation flight of wind-dispersal plant seeds. More deliberate effort was performed to improve the accuracy of the CG point calculation as follows.

The whole seed was dissected into the two parts, seed embryo (left part of y_{cut} in Fig. 3) and seed blade (right part of y_{cut} in Fig. 3), and the mass of each part was measured. The mass of the embryo part was 29 mg, and the mass of the seed blade was 4 mg. The volumes of the dissected two parts were obtained from the 3D

scan data of the seed by using the software CATIA. The volumes of the embryo part and the blade part were 30.71 mm^3 and 18.16 mm^3, respectively. Then the density of each part was calculated from the known mass and volume of each part. The density of the embryo part was calculated to be 944 kg/m^3, and the density of the blade part was calculated to be 220 kg/m^3. Therefore, the density of the seed embryo is greater 4.29 times than the density of the seed blade. The density of the seed embryo part was checked by buoyancy test and to be accurate. The volume centroids of the two parts were considered as the CG points of the two parts, and the CG point of the whole seed was then calculated from the CG points of the two parts. Figure 3 shows the CG points of the two cases for the sample seed, the case of uniform density throughout the whole seed and the case of two different density for the dissected parts. The non-uniform density case predicts the CG point of the whole seed at 18.9% span from the tip of the seed base and 31.4% local chord from the leading edge. The uniform density case predicts the CG point of the whole seed at 28.9% span and 40.4% local chord. Norberg [5] argued that the CG points of the autorotating plant seeds located at 10-20% span and 27-35% chord positions. The CG point calculation from the dissection of just two part executed in the present study may not be exactly accurate because most of the thick and rigid vascular bundles were distributed near the leading edge, and the density difference between the vascular bundles and the blade membrane was not accounted. However, it is observed that the assignment of just two different density for the embryo and the blade adopted in the present study brings the CG position to the envelope of CG points reported in the previous studies.

A : CG of uniform density case, B : CG of non-uniform density case
b=22.8 mm, c_1=5.66 mm, c_2=5.92 mm, x_1=1.78 mm, x_2=2.39 mm, y_1=4.3 mm, y_{cut}=5.47 mm, y_2=6.6 mm
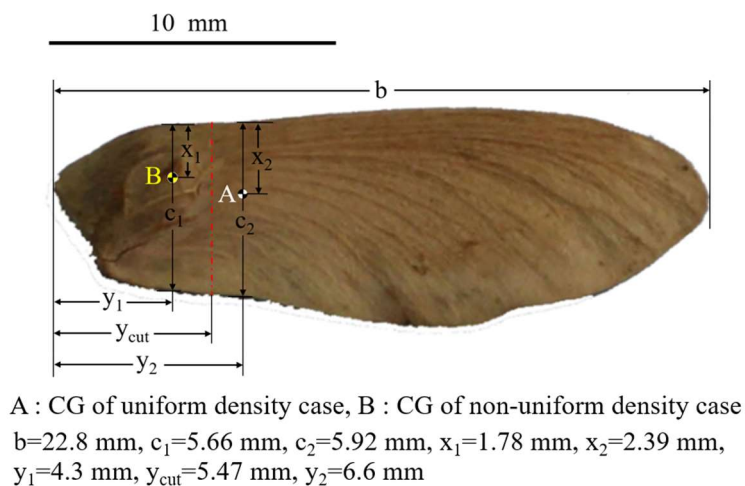
Fig. 3 Comparison of CG positions for the uniform and non-uniform density assumption

2.3 Numerical procedures for the simulation of autorotative flight

The present study performed a 6-degree-of-freedom (6DOF) simulation of the autorotative flight of maple seeds. The flow field around the seed and the aerodynamic force acting on the seed were calculated by using the Navier-Stokes equations and 6DOF motion of the autorotating seed was solved simultaneously. The Dynamic Fluid-Body Interaction (DFBI) model in the commercial "STAR-CCM+" was used as the tool of the 6DOF simulation. DFBI model allows coupled simulation of flow around a rigid body and body motion due to external and flow-induced forces. Equations of motion for the body are solved using 2nd-order discretization and implicit coupling with flow equations.

Figure 4 shows the numerical procedure of the present study. The procedures in the dotted red-colored box is the DFBI model in the STAR-CCM+. The first step of the 6DOF procedure is the measurement and calculation of the physical property of the seed such as the body geometry, mass, position of CG point and moment of inertia of the seed about the coordinate system selected. The second step is to decide the domain of simulation and the position of the body in this domain, and to generate the overset mesh. The overset mesh interface is used to couple the overset regions with the background region. The third step is to decide the simulation conditions such as the time-step size, the number of inner iterations, and the time limit of motion. All of these procedures are completed, then the DFBI model is activated.
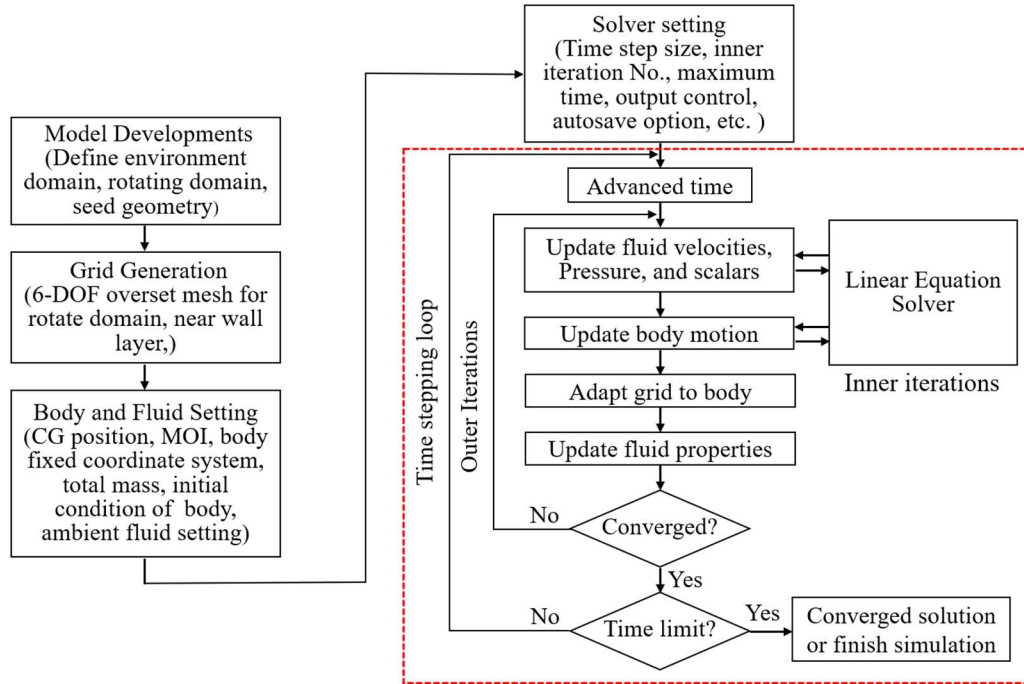
Fig. 4 Numerical procedure of 6- degree-of-freedom simulation

A 3D incompressible flow was numerically simulated using the commercial solver (STAR-CCM+). The second-order upwind scheme was used in numerical discretization. The following are the governing equations for the flow field calculation used in this study.

$$\nabla \cdot \left(\rho \vec{v} \right) = 0 \qquad (4)$$

$$\frac{\partial}{\partial t} \left(\rho \vec{v} \right) + \nabla \cdot \left(\rho \vec{v} \vec{v} \right) = -\nabla p + \nabla \cdot \left(\overline{\overline{\tau}} \right) \qquad (5)$$

where p is static pressure, $\overline{\overline{\tau}}$ is stress tensor.
The stress tensor $\overline{\overline{\tau}}$ is given by

$$\overline{\overline{\tau}} = \mu \left[\left(\nabla \vec{v} + \nabla \vec{v}^T \right) - \frac{2}{3} \nabla \cdot \vec{v} I \right] \qquad (6)$$

where μ is the molecular viscosity and I is a unit tensor.

The polyhedral grids for numerical calculation was generated from the surface node data obtained from the 3D CT image of the sample seed using Star-CCM+. In order to resolve flow near the seed surface, 8 prism layers of 0.2 mm in total thickness with an incremental rate of 1.1. The total number of grids was approximately 3,600,000. The spinning motion of the seed was implemented in the numerical simulation using multiple reference frame (MRF) method. The spinning rate was applied to the inner grids and descent velocity was applied to both of inner and outer grids. Grid refinement test was performed to find optimum number of grids, which guarantees the accuracy of the flow field calculation and takes a practical computing time.

2.4 Design of artificial seed

The autorotative flight of plant seeds is carried out solely by a fixed configuration without any active actuator. Therefore, it can be said that configuration characteristics of plant seeds governs the whole motion parameters of their autorotative flights. CG position, wing loading, camberline of the chordwise-section, planform, and surface structure have been known as the configuration characteristics governing the

autorotative flight of plant seeds [5][6]. Several studies were performed theoretically and experimentally to investigate the influence of the configuration characteristics on the autorotative flight of plant seeds. Yasuda and Azuma [6] performed an experimental study with the CG-adjustable artificial seed. They reported that there existed a CG envelope of autorotative flight feasible, and the backward movement of the CG position decreased the spinning rate of the autorotative flight. For some planform and surface roughness, the CG position of autorotative flight feasible was found to be located outside the plane of the seed surface in the Yasuda and Azuma's study. Yasuda and Azuma did not present any physical explanation how different CG position and planform of the seed changed the motion parameters of the autorotative flight, such as the spinning rate, the descent velocity, and the coning angle. The physical explanation for the interrelation between the configuration characteristics and the motion parameters of the autorotative flight of plant seeds is urgently needed. The present study performed a 6DOF simulation to get the physics of the interrelation between the configuration characteristics and the motion parameters of the autorotative flight of plant seeds. For this 6DOF simulation, an artificial seed is convenient, which can assess separately the effect of the various configuration characteristics such as the CG point, the planform shape, and the surface. An artificial seed is designed in the present study as follows.

The base line geometry of the artificial seed was the sample natural maple seed described in the section 2.1. The planform shape and the mass composition of the artificial seed were adopted from the sample maple seed. Therefore, the planform area, the mass, and the wing loading of the artificial seed were 130.5 mm^2, 33 mg and 2.48 N/m^2, respectively. The surface structure of the seed and the shape of the embryo of the artificial seed were made simply. The artificial seed was composed of the seed blade and the embryo part as shown in Fig. 5a and b. The seed blade was design as the tapered flat plate (Fig. 5c). The leading edge and the seed base tip had the largest thickness of 0.28 mm and the thickness of the seed blade decreased linearly as approaching the trailing edge and the seed tip where the thickness is 0.14 mm. The blade part of the artificial seed has the volume 16.38 mm^3, and 4 mg was assigned to its mass. The embryo part consists of the outer ball and the inner ball of the ellipsoidal shape with the dimension shown in Fig. 5d. The outer ball forms the embryo shape, and the inner ball exists completely inside the outer ball and it performs the role of CG position control. The outer ball had the volume of 39.63 mm^3, and 11.44 mg was assigned to its mass. The inner ball had the volume of 4.02 mm^3, and 17.56 mg was assigned to its mass. Therefore, the total mass of the outer and inner balls which forms the embryo of the artificial seed becomes 29 mg. And the total mass of the artificial seed is 33 mg and the total volume is 56.01 mm^3 (39.63 mm^3+16.38 mm^3).

$h_1=2c=2.9$ mm, $h_2=(0.45)(2c)=1.305$ mm

(a) (b)

$t_{LE}=0.28$ mm, $t_{LE}=0.14$ mm,
$t_{Root}=0.28$ mm, $t_{Tip}=0.14$ mm,

Outer ball : a=3.23 mm, b=2.02 mm, c= 1.45 mm
Inner ball : a=2 mm, b=0.6 mm, c=0.8 mm

(c) (d)
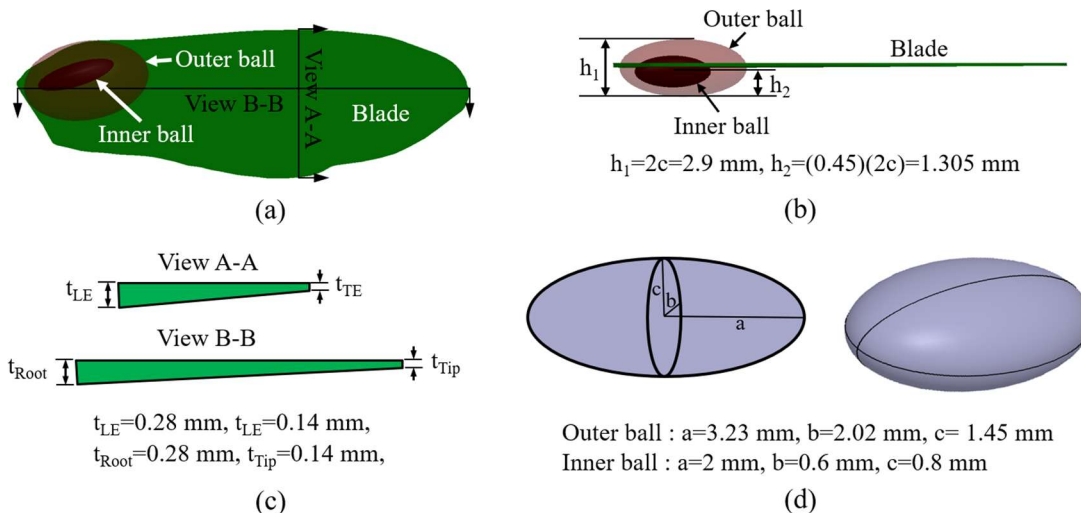
Fig. 5 Design of artificial seed, (a) Planform view of whole seed, (b) Vertical view of whole seed, (c) Seed blade and thickness distribution, (d) Dimension of outer and inner balls representing embryo part

By this design, the CG point of the artificial seed can be changed by just moving the inner ball completely inside the outer ball without any change of the whole seed configuration which will affect the aerodynamic forces. The CG point of the designed artificial seed can be moved from about 27% to 45.3% chord positions when the span position of the CG point is fixed at 18%. The moment of inertia is the important

physical property in the autorotative flight of plant seeds. The moment of inertia of the designed artificial seed was compared with that of the sample natural seed. For the natural sample seed, the moment of inertia about the pitching axis (span axis), the moment of inertia about the spinning axis (vertical axis), and the moment of inertia about the flapping axis (axis normal to the span and vertical axes) at the CG point at 18% span and 35% chord were 4.941×10^{-11} kg·m^2, 4.908×10^{-10} kg·m^2, and 4.754×10^{-10} kg·m^2, respectively. For the artificial seed, they were 5.134×10^{-11} kg·m^2, 4.304×10^{-10} kg·m^2, and 3.942×10^{-10} kg·m^2, respectively. The moments of inertia about the CG point of the designed artificial seed is not much deviated from those of the sample natural seed. The designed artificial seed is considered to have the sufficient physical property to analyze the effect of the CG point while keeping the important geometrical property of the sample natural seed, and lessening the coupling effect of the various configuration characteristics on the motion parameters of the autorotative flight of plant seeds.

3 Results and Discussion

3.1 6DOF simulation of real maple seed

6DOF simulation of the sample maple seed was performed to validate the accuracy of the tool employed (DFBI model in STAR-CCM+) and to obtain the physics of autorotative flight of natural maple seeds. The measured dimensions and the body geometry of the sample maple seed described in the section 2.1 were used as the required input data for the body information (the physical property and the 3D configuration data of the body). The motion parameters of this 6DOF simulation were compared with those of the sample maple seed measured as described in the section 2.1. Table 1 summarizes the converged motion parameters of the autorotative flight for the 6DOF simulation of the sample maple seed. With the improved CG point based on the non-uniform density assumption (18.9% span and 31.4% chord), the descent velocity, the spinning rate, and the coning angle of the 6DOF are 1.05 m/s, 136.5 rad/s, and 24.5°, respectively. The measured descent velocity, spinning rate, and coning angles were 0.906 m/s, 130.0 rad/s, and 23.2°, respectively. The deviations of the descent velocity, the spinning rate and the coning angle from the measured data are 16.0%, 5.0%, and 5.6%, respectively. With the CG point based on the assumption of the uniform density throughout the whole seed (28.9% span and 40.4% chord), the descent velocity, the spinning rate, and the coning angle of the 6DOF simulation are 1.27 m/s, 80.7 rad/s, and 14.4°, respectively. These motion parameters of the 6DOF simulation with the CG point based on the assumption of the uniform density, especially the spinning rate, deviate much from those measured for the sample maple seed. The pitch angle (-1.95°) of the 6DOF simulation with the improved CG point is also within the range of pitch angles reported in the previous studies [3][4].

The measured values of the dimensionless descent velocity ($U_T=V_D/u_g$) and the dimensionless spinning rate ($\Omega_T=C\Omega/u_g$) defined in Lee and Choi' study [10] are 0.2202 and 0.2208 for the sample natural seed of the present study when the characteristic velocity ($u_g=[(\rho-1)Cg]^{1/2}$ of 4.11 m/s is used (the density ratio (ρ) is 562.1 and the mean chord (C) is 6.98 mm). The dimensionless descent velocity and the dimensionless spinning rate are 0.2555 and 0.2318 for the 6DOF simulation of the present study with the improved CG point prediction. It is observed that the 6DOF simulation of the present study with the improved CG point predicts the motion parameters of the autorotative flight of the sample maple seed with a reasonable accuracy. The 6DOF simulation for the sample natural seed of the present study confirms that the position of the CG point is very influential to the autorotative flight of plant seeds. Therefore, an accurate prediction of the CG point is very important in the simulation of the autorotative flight of plant seeds.

Table 1 Comparison of motion parameters of the 6DOF simulation of the sample natural seed

Case	Motion parameters			
	V_D [m/s]	Ω [rad/s]	β [deg.]	θ [deg.]
Free fall measurement	0.905	130.0	23.2	x
6DOF with non-uniform density	1.05	136.5	24.5	-1.95
6DOF with uniform density	1.27	80.7	14.4	-1.68

Figure 6 shows the time histories of the motion parameters of the 6DOF simulations for the two CG points of the present study. It is observed that the sample maple seed enters into a quasi-steady state autorotation after fluctuating transient period both for the two CG points. The seed initially experiences a free-fall with the attitude of the embryo part heading vertically downward (coning angle of nearly 90°) started from the horizontal attitude (coning angle of 0°) as shown in Fig. 6c, and the spinning rate is almost zero at this time of motion as shown in Fig. 6b. For the case of the improved CG point prediction, the seed starts to spin at about 0.2 sec and thereafter its spinning rate rapidly increases up to about 160 rad/sec. The coning angle rapidly decreases during this period of spinning acceleration, and becomes about 24° at 0.3 sec. The spinning rate of the seed resurges up to about 272 rad/sec at the time of 0.35 sec. The spinning rate and the coning angle are stabilized after this time and reaches a quasi-steady state at the values of 136.5 rad/sec and 24.5°. The descent velocity experiences more simple variation as shown in Fig. 6a. It rapidly increases at the period of free-fall without spinning, but decelerates rapidly with the increase of the spinning rate, and reaches a converged value of 1.05 m/sec after the time of about 0.6 sec. The time history of pitch angle (Fig. 6d) fluctuates more with complex pattern. It experiences a transient period of large fluctuation and enters into a quasi-steady state. The pitch angle fluctuates from about -52° to about 30° during the transient period. The half-period of the big fluctuation during the time of 0 sec and 0.3 sec is about 0.1 sec. The fluctuation of the pitch angle lessens after about 0.5 sec and reaches the quasi-steady state value of -1.95° after about 0.8 sec.

For the case of CG point of uniform density assumption, the transient period of each motion parameter becomes long compared with that of the case of CG point of non-uniform density assumption. The fluctuation of the pitch angle is uneven and its amplitude is relatively large even after 1.0 sec. There exists no converged
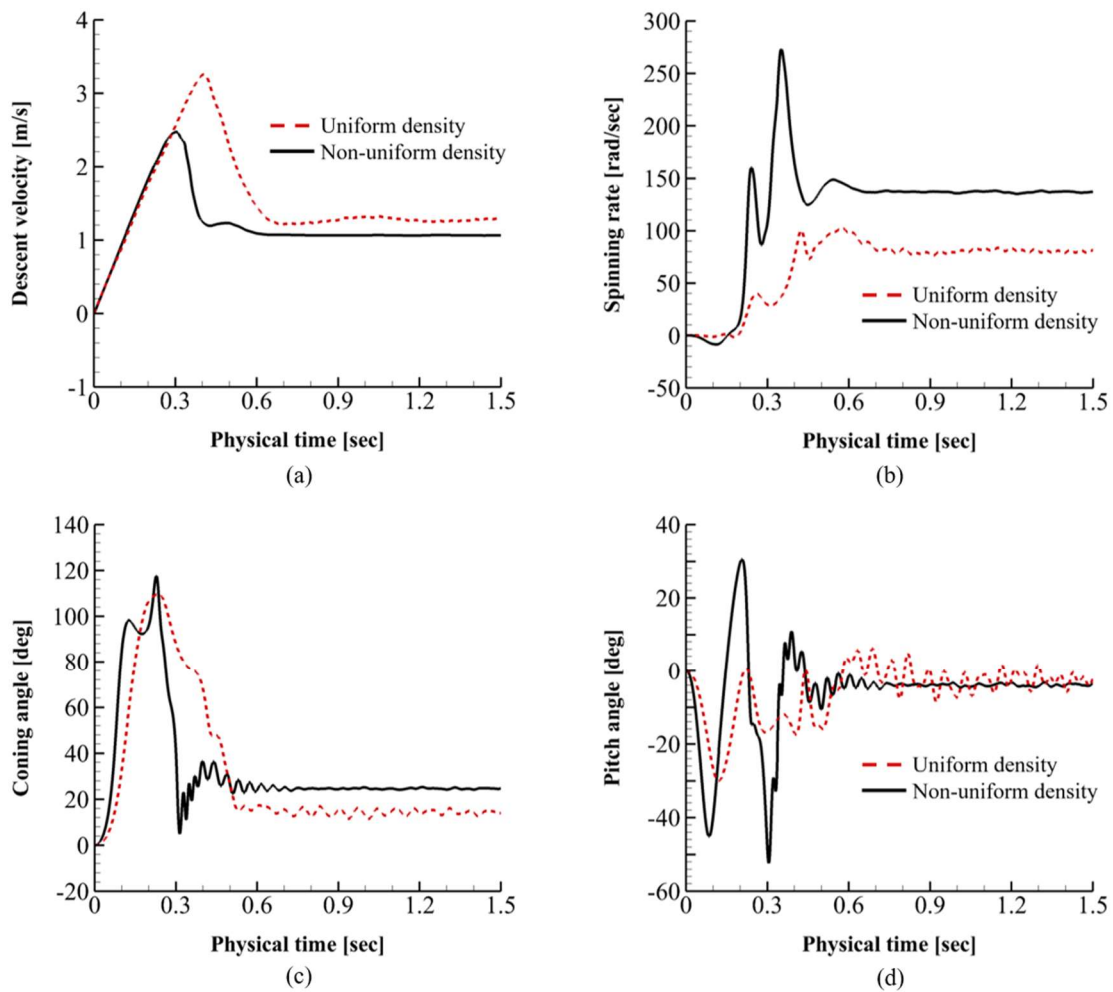
Fig. 6 Time history of motion parameters of the 6-DOF simulation of the sample natural seed,

(a) Descent velocity, (b) Spinning rate, (c) Coning angle, (d) Pitch angle

nor stable autorotation in a rigorous sense. In addition, the converged spinning rate (80.7 rad/sec) and coning angle (14.4°) are too low compared with those of the experimental measurement. The CG point of the uniform density assumption (28.9% span and 40.4% chord) is considered to be inaccurate.

Figure 7 shows the sectional streamlines, spanwise vorticity contour, and surface pressure contour for the sample maple seed. Prominent LEV is observed in the leeward region of the seed (Fig. 7a and b). The compact LEV at the inboard span positions (0.25R and 0.50R with R as the radius of spinning) causes a large suction pressure on the leeward surface of the seed blade (Fig. 7c). The highest suction pressure particularly occurs in the narrow region near the leading edge from approximately one quarter to three-quarter spans from the base tip of the seed. This matches the location of the strong and compact LEV.
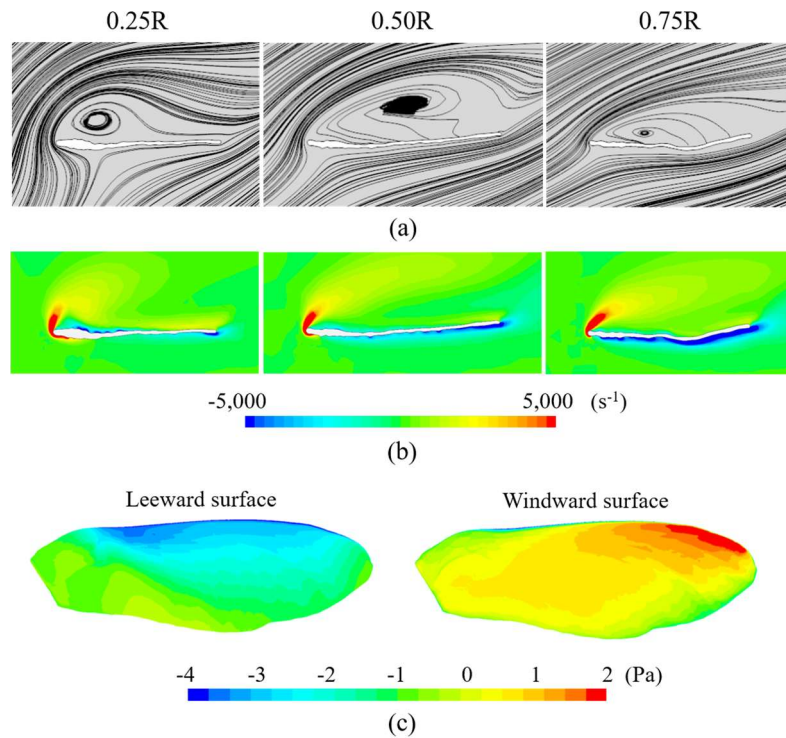
Fig. 7 Flow pattern and surface pressure distribution of the sample natural seed in autorotative flight, (a) Sectional streamlines, (b) Spanwise vorticity contour, (c) Surface pressure contour

Figure 8 shows the spanwise velocity, the spanwise transport of vorticity ($v \cdot \omega_y$), and the three-dimensional flow structure. A spanwise flow is formed over the leeward surface of the seed blade (Fig. 8a), and the spanwise transport of vorticity in the LEV, which presides over the leeward region of the seed (Fig. 8b), is clearly observed. The spanwise flow and the spanwise transport of vorticity over the leeward surface of the seed blade observed in Fig. 8, are consistent with the results of the experimental study for the artificial maple seeds of Lentink et al. [3] and the experimental study of the real maple seed of Lee et al. [8]. The attached LEV is possible by the strong spanwise flow over the leeward surface of the seed blade, which drains vorticity from the LEV toward the wingtip vortex and prevents the LEV to grow large and become unstable. The 3-dimensional flow structure (Fig. 8c) shows that the LEV was the spanwise-spiraling vortex. The spanwise-spiraling vortex flow and the spanwise transport of vorticity are considered as the key mechanism which makes the LEVs be stable and attached onto the seed surface even at very high angles of attack ($\alpha \approx 54°$ at 0.25R, $\alpha \approx 35°$ at 0.50R). The role and the behavior of the LEV in the autorotative flight of maple seeds are reported elsewhere [12]. Also the analysis of the effect of the motion parameters such as the pitch angle, the coning angle, and the advance ratio on the aerodynamics of the autorotating maple seeds, is in being prepared as another paper.
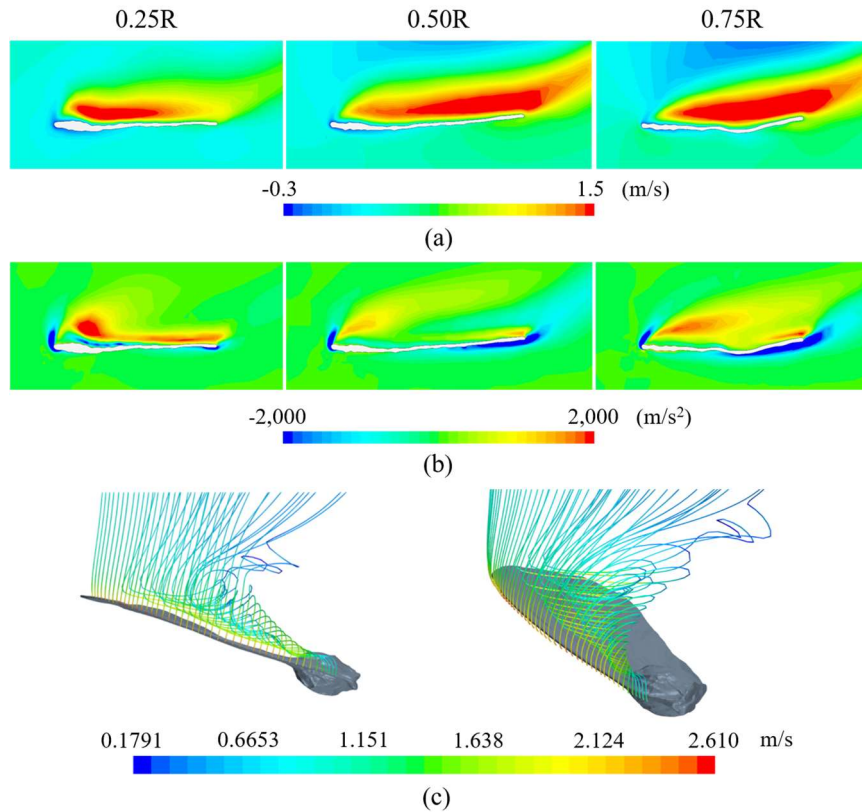
Fig. 8 Flow pattern of the sample natural seed in the autorotative flight, (a) Spanwise velocity contour, (b) Spanwise transport of vorticity contour, (c) Three-dimensional flow structure

3.2 6-DOF simulation of artificial seeds

The body configuration and structure of plant seeds solely determine their autorotative flight characteristics. The present study performed 6DOF simulations using the artificial seed described in the section 2.4, which is convenient to investigate the effect of the CG point, the planform shape, and the surface structure on the autorotative flight of plant seeds while keeping the important geometrical property of the sample natural seed, and lessening the coupling effect of the various configuration characteristics on the motion parameters of the autorotative flight of plant seeds. The effect of the CG point that is the most configuration characteristics, is analyzed first. Five different CG positions, 27, 31, 35, 39, and 43% local chord, were simulated at the fixed 18% span position, and four different CG positions, 15, 18, 21, and 24% span, were simulated at the fixed 35% chord position. Figure 9 shows the CG points for the 6DOF simulation of the artificial seed in the present study.
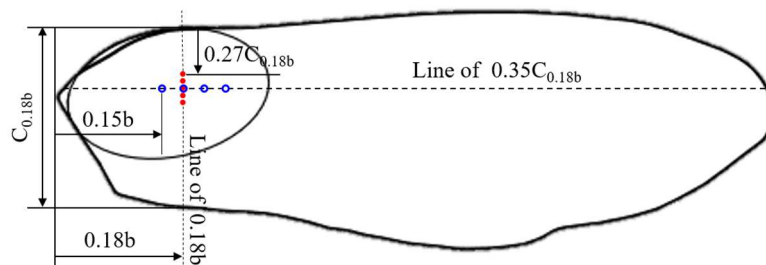
Fig. 9 CG positions for 6DOF simulation of the artificial seed

Table 2 summarizes the converged motion parameters of the autorotative flight for the 6DOF simulation of the artificial seed as varying the CG position in the chordwise direction. It is observed that the spinning rate and the magnitude of the pitch angle (which is always negative) decrease as the CG point (which coincides

with the position of the spin axis) moves toward the leading edge. The coning angle increases as the CG point moves toward the trailing edge. The descent velocity increases from 1.081 m/sec to 1.46 m/sec when the CG point moves from 27% chord to 43% chord. However, the change of the descent velocity is minor for the 27, 31 and 35% chord positions. The coning angle (42.0°) at the 43% chord position eludes the typical range (15° to 30°) for the coning angles of the autorotating maple seeds reported. The descent velocity (1.46 m/sec) at the 43% chord position is also too high when considering the value of wing loading of the seed simulated (2.48 N/m²). This observation exhibits that the CG point of 18% span and 43% chord may be not realistic or not be chosen in the autorotative flight of plant seeds in nature, even though the autorotative flight is possible.

Table 2 Comparison of motion parameters at different chord positions of CG (18% span)

% Chord of CG position	Motion parameters			
	V_D [m/s]	Ω [rad/s]	β [deg.]	θ [deg.]
27	1.081	165.9	18.6	-7.58
31	1.049	159.1	19.1	-6.95
35	1.045	146.8	23.5	-4.71
39	1.136	131.5	32.3	-2.49
43	1.46	124.0	42.0	- 1.45
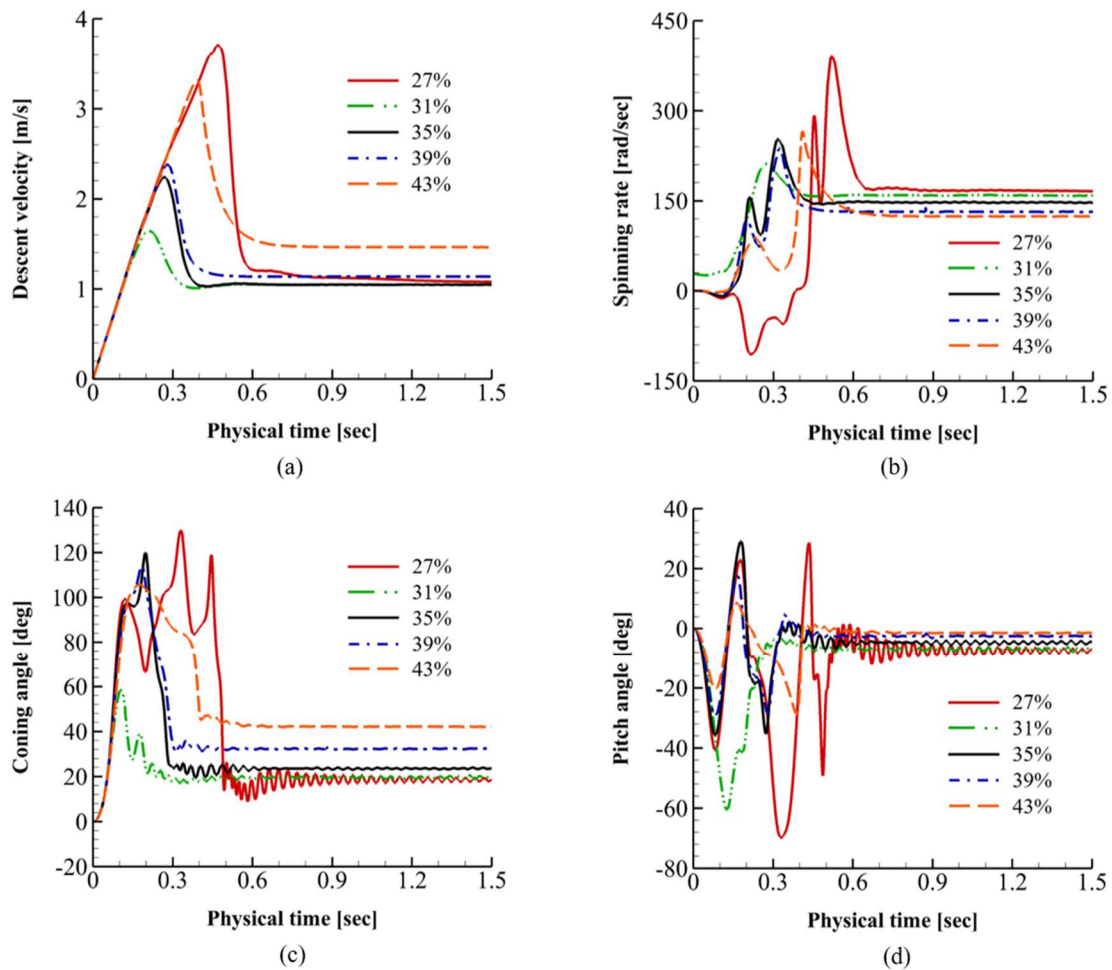
Fig. 10 Time history of motion parameters for different chord positions of the CG point (18% span),

(a) Descent velocity, (b) Spinning rate, (c) Coning angle, (d) Pitch angle

Figure 10 compares the time histories of the motion parameters of the 6DOF simulations for different chordwise CG points. The entrance into the quasi-steady state after fluctuating transient period is same as in the 6DOF simulation for the sample natural seed. The spinning rate, the coning angle, and the pitch angle fluctuate with large amplitude during the transient period before entering into the quasi-steady state (or stable) period. The fluctuations of the motion parameters diminish as the autorotative flight proceeds, and all four motion parameters enter into the quasi-steady state within 0.7 sec after release for the all 5 CG positions. The fluctuating amplitudes of the motion parameters are largest at the 27% chord position. The fluctuations of the motion parameters become smaller as the CG point moves backward. The accompanying time tendency of the spinning rate and the coning angle is the same as in the 6DOF simulation of the sample natural seed.

The seeds do not fall straight, but drift in the horizontal plane during the autorotating descent. However, the drift was not large except the 27% chord position. The trajectory of the CG point was monitored. Figure 11 shows the trajectories of the CG points for the various chordwise CG positions. It is observed that the drifts in the x- and y-directions are smaller than 13 mm during the fall distance of 2.1 m for all of the 31, 35, 39, and 43% CG positions (Fig. 11a and b). For the case of 35% CG positions (Fig. 11c and d), the drift in the x-direction is smaller than 0.9 mm and the drift in the y-direction is smaller than 2.2 mm after 0.6 sec when the seed entered into the stable period of the autorotative flight.
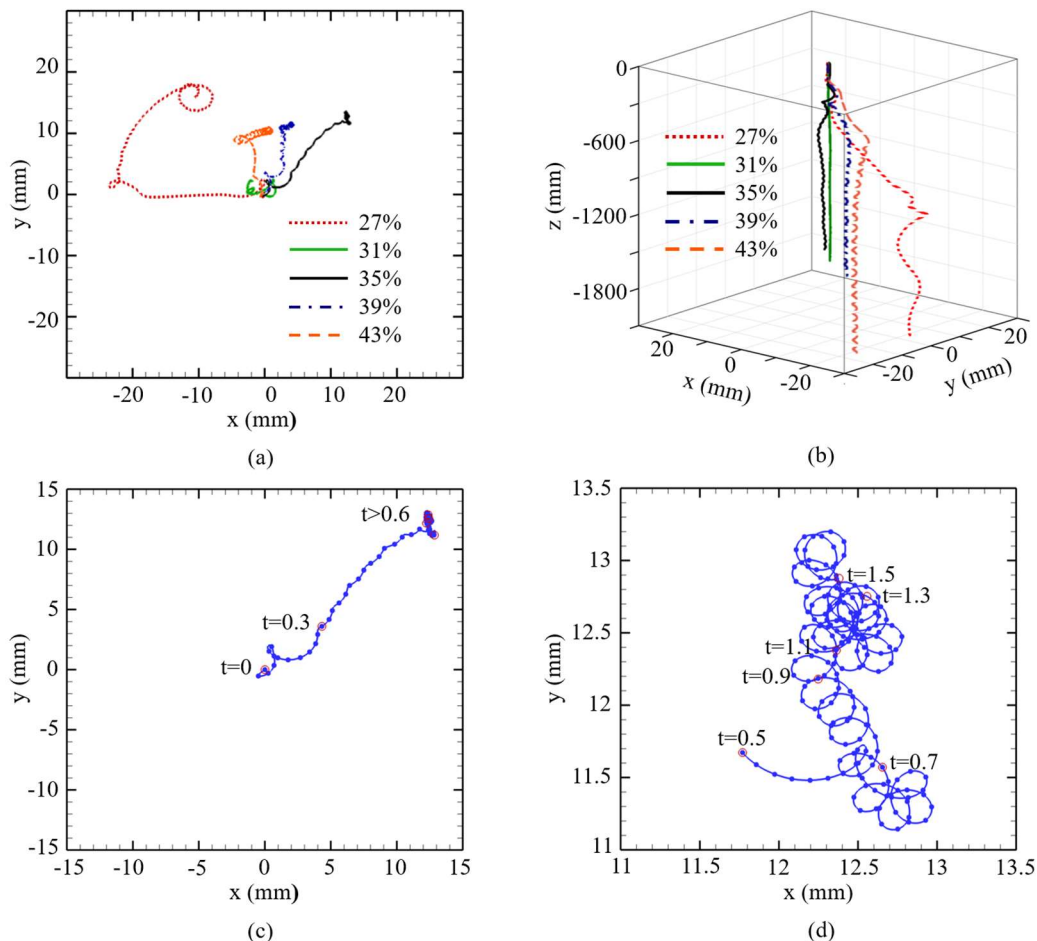
Fig. 11 Trajectory of the CG points, (a) Trajectory in the horizontal plane, (b) Trajectory in the vertical plane, (c) Trajectory in the horizontal plane for the 35% case, (d) Enlarged trajectory in the horizontal plane for the 35% case

Autorotative flight of plant seeds is the result of a delicate equilibrium between the gravity (weight of the seed), the inertial force, and the aerodynamic force. The gravity provides the seed driving energy of motion and the aerodynamic force generated by the relative wind passing the seed, spins the seed and decelerates the free-falling velocity. The centrifugal force caused by the spinning motion of the seed about the vertical axis

balances the radial component of the aerodynamic force acting on the seed blade. An equilibrium coning angle is established at the balance of the centrifugal force, the moment of the distributed weight of the seed blade, and the aerodynamic force as expressed in Fig. 1 and Eq. 3. Keeping this motion physics in mind and referencing Fig. 1, the characteristics of the autorotative flight observed in Figs. 10 and 11 is explained as follows.

As the CG point, which coincides the spinning axis, moves toward the leading edge, the moment about the pitch axis (span axis) increases in the negative direction (pitch-down direction) due to the increase of the moment arm of the aerodynamic force (mainly normal force) acting on the seed blade. This increase of the pitching moment in the negative direction then increases the pitch angle in the negative direction. The increase of the pitch angle in the negative direction tilts the aerodynamic force vector forward, and the accelerating spinning torque component (dLsinφ in Eq. 2) increases and the spin rate increases. As the spin rate increase the coning angle decreases due to the increased centrifugal force. And the increased upward component of the aerodynamic force caused by the decrease of the coning angle, decelerates the descent velocity.

The interrelation between the motion parameters is substantiated by tracing the moments about the three axes and the related motion parameters during the whole motion period of the seed. Figure 12 shows the time traces of the moments about the three axes, the pitching, spinning, and flapping axes and the related motion parameters for the 35% chord CG position. As shown in Fig. 12a, y-axis (span axis) is the pitching axis, z-axis (vertical axis) is the spinning axis, and x-axis is the flapping axis. The three moments M_x, M_y, and M_z of Fig. 12 are moments about the body-fixed coordinates, x, y and z, as shown in Fig. 12a.
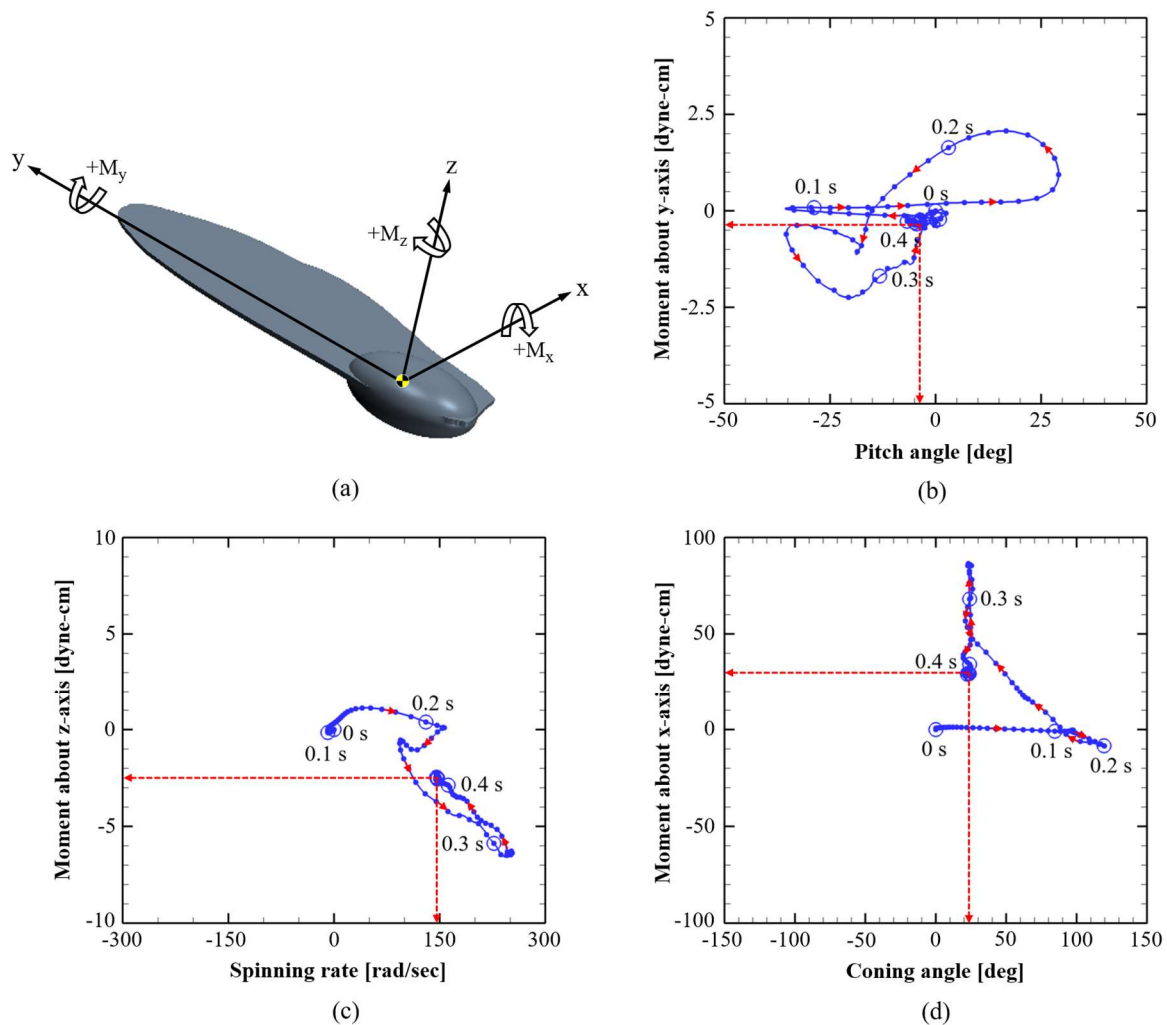
Fig. 12 Time history of the related moment and motion parameter for the 35% CG case, (a) Definition of positive moment, (b) Moment about the span axis (y-axis and the pitch angle, (c) Moment about the vertical axis (z-axis) and the spinning rate, (d) Moment about the flapping axis (x-axis) and the coning angle

The pitch angle and the pitching moment are initially zero. As shown in Fig. 12b, the seed obtains the negative value of large magnitude with the almost zero pitching moment as soon as the seed starts fall. Then the seed changes the pitch attitude abruptly, and the pitch angle starts to increase in the positive direction with the positive pitching moment of small magnitude from 0.1 sec to 0.15 sec. The pitch angle obtains the maximum value of about 29°, and starts to decrease from 0.15 sec to 0.2 sec. During this period of motion, the positive pitching moment increases up to the value of 0.21 dyne·cm and then starts to decrease. The pitching moment decreases continuously and enters into the negative region. Thereafter (after about 0.4 sec) the pitching moment and the pitch angle never return to the positive region. Finally, the pitching moment and pitch angle remain in the stabilized zone where the fluctuations of the moment and angle are very small. At this period of the autorotative flight, the pitch angle becomes -4.71°, and this pitch angle is supported by M_y of about -0.3 dyne·cm as indicated with the red-colored arrows in Fig. 12b.

The time traces of the moment about the vertical axis and the spinning rate are shown in Fig. 12c. The moment about the z-axis and the spinning rate start with zero value (no initial rotation). There are almost zero z-axis moment and spinning rate during the motion period of 0 sec to 0.1 sec. This means that the seed falls almost vertically without any rotation. The seed obtains the positive z-axis moment of small magnitude and the spinning rate increases during the time of 0.1 sec to 0.2 sec. After 0.216 sec, the seed starts to obtain the negative z-axis moment and this negative z-axis moment decreases up to the value of about -6.6 dyne·cm at the time of 0.32 sec as shown in Fig. 12c. The spinning rate becomes about 250 rad/sec at the time of 0.32 sec. The magnitudes of the negative z-axis moment and the spinning rate decrease after 0.32 sec, and M_z and the spinning rate settle down in the stabilized zone after 0.4 sec. At this stabilized period of the autorotative flight, the spinning rate becomes 146.8 rad/s, and this spinning rate is provided by M_z of -2.55 dyne·cm as indicated with the red-colored arrows in Fig. 12c.

The coning angle increases from 0° to 85° during the motion period of 0 sec and 0.1 sec with almost zero flapping moment as shown in Fig. 12d. This means that the seed falls almost vertically with the seed base heading the earth surface. The flapping moment starts to increase continuously after 0.2 sec, and it reaches to the value of about 88 dyne·cm. Thereafter M_x rapidly decreases and it enters into the stabilized zone after 0.4 sec. The coning angle fluctuates with very small amplitude during the motion period of 0.3 sec to 0.4 sec when the flapping moment decreases rapidly. At the final stabilized motion period, the coning angle becomes 23.5°, and this coning angle is supported by the M_x of 30 dyne·cm as indicated with the red-colored arrows in Fig. 12d. It is observed that the flapping moment has about ten-times greater order-of-magnitude than the pitching and the spinning moment. This is due to the geometric characteristics of the autorotating plant seeds which have the relatively long span and therefore the large moment arm about the flapping axis.

The effect of the CG point movement in the spanwise direction is also investigated. Table 3 summarizes the converged motion parameters of the autorotative flight for the 6DOF simulation of the artificial seed as varying the CG position in the spanwise direction. As the CG point (which coincides with the position of the spin axis) moves toward the seed blade tip, the spinning rate and the descent velocity at the stable increase. But the increase rate of the descent velocity is insignificant. The coning and pitch angles also change as the CG point moves toward the seed blade tip. However, the change of the coning and pitch angles are very small and do not have the consistency compared to the case of the chordwise movement of the CG point.

Table 3 Comparison of motion parameters at different span positions of CG (35% chord)

% Span of CG position	Motion parameters			
	V_D [m/s]	Ω [rad/s]	β [deg.]	θ [deg.]
15	1.012	138.8	23.2	-4.24
18	1.045	146.8	23.6	-4.71
21	1.079	154.5	22.7	-5.24
24	1.117	152.8	21.4	-5.20

Figure 13 compares the time histories of the motion parameters for the four CG positions in the spanwise direction. The artificial maple seed enters into a quasi-steady state autorotation after fluctuating transient period. It is observed that the fluctuations of the motion parameters during transient period are small compared to the case of the chordwise movement of the CG point, and the values of the motion parameters at the stable period are not much different for the four spanwise CG positions selected. The variation patterns of the motion parameters during the transient periods of the four CG positions are almost same. This fact shows that the effect of the CG point movement in the spanwise direction on the autorotative flight is small at least within the range of the spanwise movement considered. The increased fluctuating amplitudes of the coning and pitch angles for the 24% span position observed in Fig. 13c and d, hint that the effect of the movement of the CG point beyond 24% span position may not be minor, and that converged or stable autorotation may not occur for the CG point beyond 24% span position. This speculation needs to be investigated.
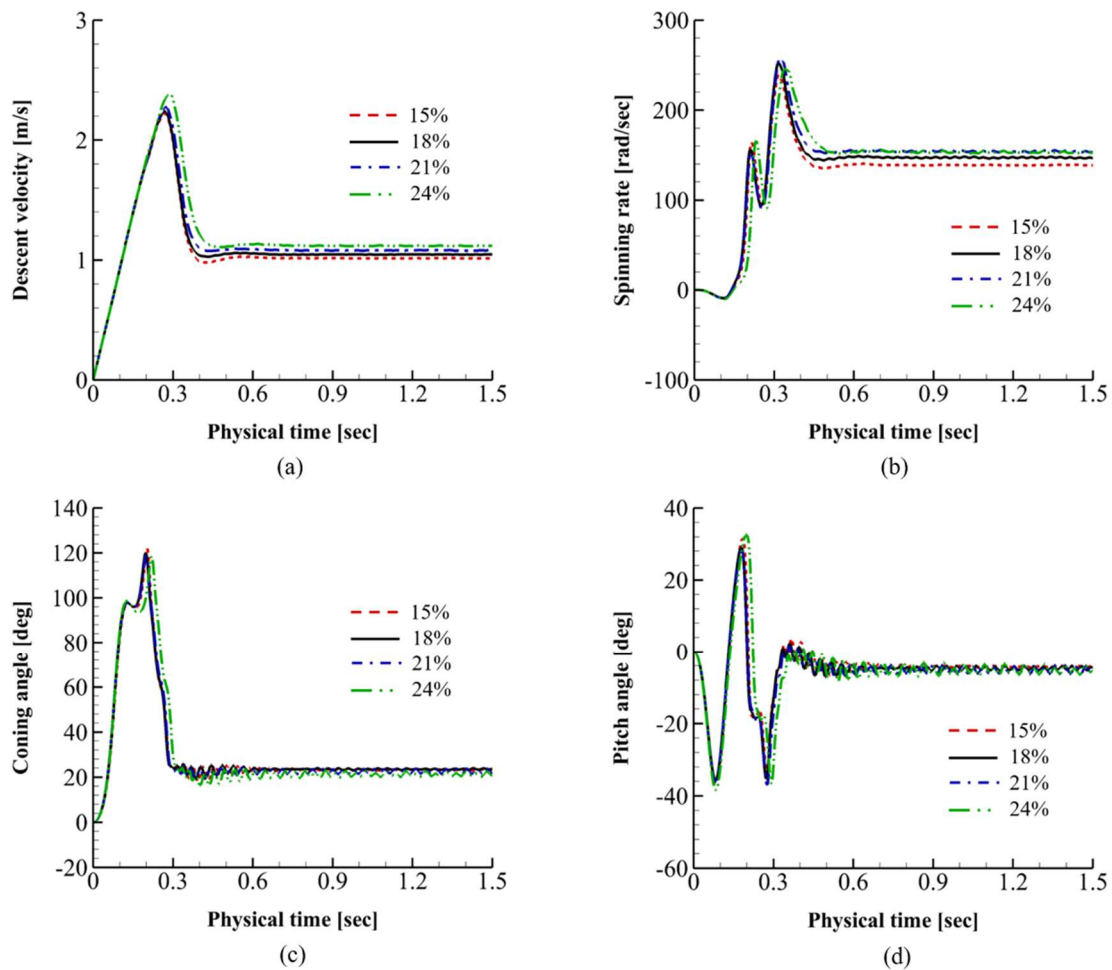
Fig. 13 Time history of motion parameters for different span positions of the CG point (35% chord),

(a) Descent velocity, (b) Spinning rate, (c) Coning angle, (d) Pitch angle

4 Conclusions

The present study performed a numerical simulation of the autorotative flight of real and artificial maple seeds to reveal the interrelation of the configuration characteristics and the motion characteristics of the autorotating plant seeds. The flow field around the seed and the aerodynamic force acting on the seed were calculated by using the Navier-Stokes equations and the 6-degree-of-freedom (6DOF) motion of the autorotating seed was solved simultaneously. The 3-dimensional (3D) configuration data of the real maple seed were obtained by using 3D optical scanning, and they were used in the calculation of the aerodynamic force acting on the seed, and to solve the 6-degree-of-freedom (6DOF) motion.

The motion parameters such as the descent velocity, the spinning rate, and the coning angle agreed reasonably well with those measured for the sample real seed. 6DOF simulation of the artificial maple seeds was also performed to investigate the effect of the position of center of gravity on the autorotative flight of maple seeds. It was found that the chordwise position of the center of gravity, which determines the value of the moment about the span axis and consequently governs the pitch angle, was the most influential factor of the configuration characteristics in the autorotative flight of maple seeds. The effect of the CG point movement in the spanwise direction was relatively minor compared to the CG point movement in the chordwise direction. The interrelation between the configuration characteristics and the motion characteristics of the autorotating maple seeds is analyzed based on the time history of the motion parameters, and the time trace of the moment about the three axes and related motion parameters of the autorotative flight.

Acknowledgements

References

[1] Bullock J M R, Kenward R, Hails E R (2002) Dispersal ecology. Blackwell, Malden, MA.

[2] Minami S, Azuma A (2003) Various flying modes of wind-dispersal seeds. *Journal Theoretical Biology*, vol. 225, pp 1-14.

[3] Lentink D, Dickson W B, van Leeuwen J L, Dickinson M H (2009) Leading-edge vortices elevate lift of autorotating plant seeds. *Science*, vol. 324, pp 1438–1440. doi.org/10.1126/science. 1174196.

[4] Azuma A, Yasuda K (1989) Flight performance of rotary seeds. *Journal of Theoretical Biology*, vol. 138, pp 23–53. doi.org/10.1016/S0022-5193(89)80176-6

[5] Norberg R (1973) Autorotation, self-stability, and structure of single-winged fruits and seeds (samaras) with comparative remarks on animal flight. *Biological Review*, vol. 48, pp 561–596. doi.org/10.1111/j.1469185X.1973.tb01569.x 2.

[6] Yasuda K, Azuma A (1997) The autorotation boundary in the flight of samaras. *Journal of Theoretical Biology*, vol. 185, pp 313– 320. doi.org/10.1006/jtbi.1996.0299

[7] Seter D, Rosen A (1992) Stability of the vertical autorotation of a single-winged samara. *Journal of Applied Mechanics*, vol. 59, pp 1000–1008. doi.org/10.1115/1.2894014

[8] Lee S J, Lee E J, Sohn M H (2014) Mechanism of autorotation flight of maple samaras (*Acer palmatum*). *Experiments in Fluids*, vol. 55, pp 1–9. doi.org/10.1007/s00348-014-1718-4

[9] Varshney K, Chang S, Wang Z J (2012) The kinematics of falling maple seeds and the initial transition to a helical motion. *Nonlinearity*, vol. 25, C1-C8

[10] Lee I, Choi H (2017) Flight of a falling maple seed. *Physical Review of Fluids*, 2, 090511. doi.org/10. 1103/PhysRevFluids.2.090511

[11] Arranz G, Moriche M, Uhlmann M, Flores O and Garc´ıa-Villalba M (2018) Kinematics and dynamics of the auto-rotation of a model winged seed. *Bioinspiration & Biomimetics*. Vol. 13, 036011. doi.org/10.1088/1748-3190/aab14

[12] Sohn M H (2018) The role and behavior of the leading edge vortex in the autorotative flight of plant seeds. In: Proceeding of the 2018 fall conference, The Korean society of visualization, November 29-30, Busan, Korea